INTERNATIONAL JOURNAL FOR NUMERICAL METHODS IN ENGINEERING
Int. J. Numer. Meth. Engng 2007; **72**:893–923
Published online 4 July 2007 in Wiley InterScience (www.interscience.wiley.com). DOI: 10.1002/nme.2030

Extrinsic cohesive modelling of dynamic fracture and microbranching instability in brittle materials

Zhengyu (Jenny) Zhang[1], Glaucio H. Paulino[1,*,†] and Waldemar Celes[2]

[1]*Department of Civil and Environmental Engineering, University of Illinois at Urbana-Champaign, Newmark Laboratory, 205 North Mathews Avenue, Urbana, IL 61801-2397, U.S.A.*
[2]*Tecgraf/PUC-Rio Computer Science Department, Pontifical Catholic University of Rio de Janeiro, Rua Marquês de São Vicente 225, Rio de Janeiro, RJ, 22450-900, Brazil*

SUMMARY

Dynamic crack microbranching processes in brittle materials are investigated by means of a computational fracture mechanics approach using the finite element method with special interface elements and a topological data structure representation. Experiments indicate presence of a limiting crack speed for dynamic crack in brittle materials as well as increasing fracture resistance with crack speed. These phenomena are numerically investigated by means of a cohesive zone model (CZM) to characterize the fracture process. A critical evaluation of intrinsic *versus* extrinsic CZMs is briefly presented, which highlights the necessity of adopting an extrinsic approach in the current analysis. A novel topology-based data structure is employed to enable fast and robust manipulation of evolving mesh information when extrinsic cohesive elements are inserted adaptively. Compared to intrinsic CZMs, which include an initial hardening segment in the traction–separation curve, extrinsic CZMs involve additional issues both in implementing the procedure and in interpreting simulation results. These include time discontinuity in stress history, fracture pattern dependence on time step control, and numerical energy balance. These issues are investigated in detail through a 'quasi-steady-state' crack propagation problem in polymethylmethacrylate. The simulation results compare reasonably well with experimental observations both globally and locally, and demonstrate certain advantageous features of the extrinsic CZM with respect to the intrinsic CZM.

Received 7 March 2006; Accepted 5 February 2007

KEY WORDS: finite element method; cohesive zone model (CZM); dynamic fracture; branching; instability; intrinsic; extrinsic; topological data structure

*Correspondence to: Glaucio H. Paulino, Department of Civil and Environmental Engineering, University of Illinois at Urbana-Champaign, Newmark Laboratory, 205 North Mathews Avenue, Urbana, IL 61801-2397, U.S.A.
†E-mail: paulino@uiuc.edu

Contract/grant sponsor: National Center for Supercomputing Applications

1. INTRODUCTION

Dynamic fracture instability in brittle materials has been a field of much interest and research during the past decades [1]. Experiments have been performed on various amorphous brittle materials to investigate dynamic fracture behaviour; for instance, Homalite-100 [2–5], Polymethylmethacrylate (PMMA) [6, 7], Solithane-113, and Polycarbonate [7]. These experiments provide valuable information for improved understanding of dynamic fracture phenomena in brittle materials, particularly with respect to the process of nucleation, growth, and coalescence of microcracks. Two phenomena remained the focus of interest among these observations: first, crack surface roughens as crack speeds up, as the 'mirror-mist-hackle' stages described in [4]; second, the onset of instability occurs at a speed well below the theoretical limiting speed predicted by classical linear elastodynamics. A dynamic fracture experiment with focus on microbranch formation in PMMA is found in [6], which further investigated the transitional stage when microbranches occur and grow longer with increasing crack speed, as shown in Figure 1. Although crack instability at high speed is predicted by the conventional linear elastodynamic theory, these experimental observations reveal significant deviation of fracture behaviour in the brittle material from those conditions suggested by the linear theory.

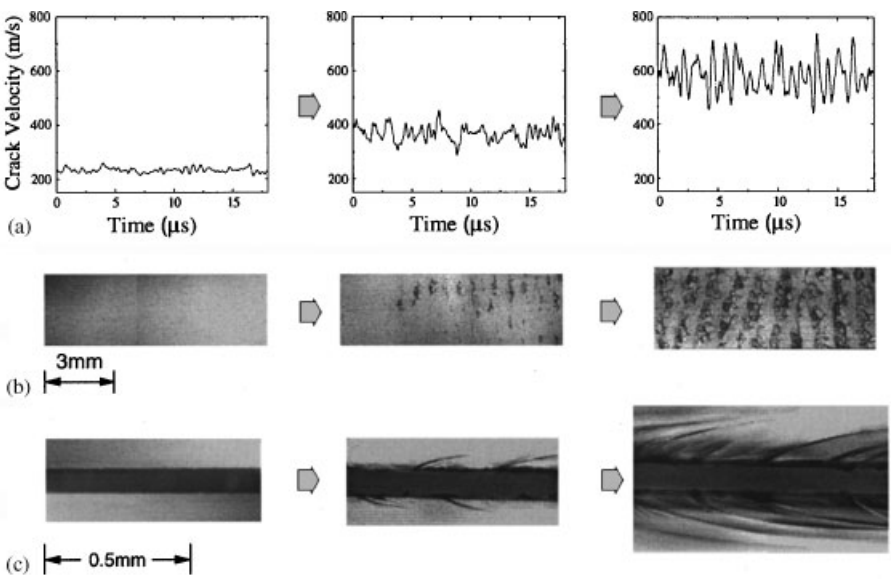

Figure 1. Experimental observation of branching instability as crack propagates in PMMA. Figure reproduced from Figure 4 of Sharon and Fineberg [6]. The critical crack speed at which microbranch appears is denoted as V_c: (a) the velocity of the crack is a smooth function of time for $V = 300\,\mathrm{m/s} < V_c$ (left), at $V = 400\ \mathrm{m/s} \approx V_c$ the crack velocity starts to oscillate (centre), the oscillation amplitudes increase at higher velocity (right); (b) for $V = 300\ \mathrm{m/s} < V_c$ the fracture surface is smooth (left), at $V \approx 400\ \mathrm{m/s}$ small regions of different texture are distributed along the surface (centre), at $V \approx 600\ \mathrm{m/s}$ these regions coalesce, forming a periodic pattern with wavelength on the order of 1 mm (right); and (c) a single crack is observed (left) for $V < V_c$. Microbranches appear at $V \approx V_c$ (centre), and increase in length at higher velocities (right).

DOI: 10.1002/nme

This work investigates dynamic crack microbranching processes by incorporating a cohesive zone model (CZM) in the finite element method to characterize the fracture process. One major challenge in simulating branching phenomena is how to allow multiple cracks to form 'freely' in a finite discretization. Among the set of numerical schemes in the literature, CZM has the advantage of allowing multiple crack formation. Between the two classes of CZMs, i.e. '*intrinsic*' and '*extrinsic*' models, the latter is adopted in the study as this approach avoids a number of disadvantages of the former, including the so-called 'artificial compliance', which may result in significant reduction of stiffness of the modelled specimen. The extrinsic CZM employed in the finite element scheme is characterized by a finite cohesive strength at onset of material weakening and work to fracture. Compared to intrinsic CZMs, which include an initial hardening segment in the traction–separation curve, extrinsic CZMs involve additional issues both in implementing the procedure and in interpreting simulation results. These include time discontinuity in stress history, fracture pattern dependence on time step control, and numerical energy balance. The implementation of the extrinsic CZM approach is facilitated by a novel data structure that allows convenient and robust access to adjacency information as well as adaptive insertion of cohesive elements during the course of the simulation [8, 9].

The remaining of the paper is organized as follows. Section 2 presents a literature review of related work, followed by a brief comparison of intrinsic and extrinsic CZMs in Section 3. Section 4 discusses the computational scheme, and Section 5 presents the topological data structure (TopS) employed in the numerical implementation. A detailed numerical example is studied in Section 6. Finally, Section 7 provides some concluding remarks of the study.

2. RELATED WORK

The analytical solution for a crack moving at constant velocity based on linear elastic fracture analysis dates back to the middle of last century [10], which predicted crack velocity limit as the Rayleigh wave speed (c_R) for mode-I problems. Such analysis assumes ideal brittle fracture model in which the crack moves at constant speed along its initial direction through an infinite strip. Freund [11] provides a more detailed description of the ideal model with further consideration of non-uniform crack tip motion. Moreover, this theoretical model also predicts dynamic crack instability. For quasi-static crack propagation, the maximum circumferential ('hoop') stress criterion predicts the deviation angle $\theta = 0$, i.e. the crack tends to propagate along the initial crack path. For dynamic crack propagation, however, the angular distribution of circumferential stress depends on crack velocity. As the crack tip velocity increases, the maximum stress may not necessarily occur at $\theta = 0$. When the crack tip velocity reaches about two-thirds of the Rayleigh wave speed, the hoop stress varies less than 10% within an angular range from -45 to 45° (see, e.g. [11, Figure 4.2]). When crack-tip velocity reaches about three-fourths of the Rayleigh wave speed, the hoop stress varies only marginally within the angular range from -60 to 60°. This solution suggests that crack path becomes unstable at high crack-tip speed and branching may occur. Although this linear elastodynamic-based analysis is significant in revealing the onset of fracture path instability, the predicted critical crack velocity does not agree well with experimental observations [4, 6, 7], which reveal that the limiting crack speed is about half of the Rayleigh wave speed, and that the specimen develops increasing fracture surface roughness with increasing fracture velocity.

Motivated by the experimental observations, Gao [12] proposed an explanation through the correlation between *micro*-crack speed and *macro*-crack speed. At high velocity, the crack tends

DOI: 10.1002/nme

to propagate through a 'wavy' path so as to maximize the energy flux into the crack tip while maintaining the average crack speed below half of the Rayleigh wave speed. The microcracks can propagate at higher speed, with the limit predicted by the Yoffe solution [10]. Gao's work [12] also pointed out the importance of 'T-stress' in the dynamic crack propagation process. A negative T-stress that is parallel to the crack path tends to stabilize the crack path along its original surface, while a positive T-stress results in the opposite behaviour. Rice *et al.* [13] later pointed out that this stabilization effect is limited; at crack velocity beyond 75% of the Rayleigh wave speed, the crack path will be destabilized and any deviation from straightness then gets amplified. Rice *et al.* [13] also observed that the analyses by Eshelby [14] and Freund [15] indicate that there is enough energy available to create two crack surfaces as was available to create one when the crack speed is about 75% of the Rayleigh wave speed.

A theory of local limiting speed was postulated by Gao [16] through consideration of non-linear elastic response at crack tip, which governs the *local* crack limiting speed. The local limiting speed is found to be $c_s\sqrt{\sigma_{\max}/\mu}$, where c_s is the macroscopic shear wave speed, μ is the shear modulus and $\sigma_{\max}$ is the equibiaxial cohesive strength of the solids. The local limiting speed provides an explanation for the onset of 'mirror-mist' transition of fracture surface. Gao [16] also developed a steady-state maximization algorithm to compute atomistic responses near the tip of a crack moving with constant speed in a 6–12 Lenard-Jones lattice. The critical velocity at the onset of local crack branching is in agreement with molecular dynamics simulation study of Abraham *et al.* [17], and is about 80% of the calculated local limiting speed.

Brittle fracture instability was also investigated through numerical means, including the finite element method (FEM) [18–20], the boundary element method (BEM) [21], and molecular dynamics [17]. Xu and Needleman [18] did FEM simulation of macrobranch occurrence in a centre-cracked plate subjected to tensile displacement loading. Their work uses intrinsic CZMs, which involve embedded interface elements in the mesh that allow separation between triangular-shaped area elements. The simulation result is significant in revealing the branching dependence on applied loading, and in qualitatively matching the experimental observations. However, the method suffers from mesh dependence and the crack speed is artificially increased due to so-called 'lift-up' effect, i.e. the cohesive interfaces along the potential crack path invariably open up to a small separation distance (even though the actual crack has not run through those interfaces yet), and a sufficiently high loading can cause instant separation of all cohesive interfaces along the path, thus resulting in spuriously high crack speed. Klein *et al.* [19] simulated microbranch occurrence using a non-linear continuum 'virtual internal bond' model, which considers material weakening at the strain localization region. The simulation produced average crack speed and microbranch pattern that qualitatively match the experimental measurements. Belytschko *et al.* [20] investigated crack bifurcation using the extended FEM (X-FEM) combined with the loss of hyperbolicity condition for the crack initiation criterion. Their work focused more on method development rather than reproducing observed experiments, and the authors pointed out that their method neither simulates roughness in the crack path, nor treats the microbranches. Rafiee *et al.* [21] employed boundary integral method to investigate the crack bifurcation and trifurcation under bi-axial loading case. The crack branching criterion used in that study is attainment of a critical stress intensity factor (SIF), which is much higher than the static material toughness. Therefore, velocity toughening effect is considered in the model. Abraham *et al.* [17] investigated crack-tip instability using molecular dynamics involving 10^6 atoms. Although at substantially smaller time and length scales, the atomistic simulation produced 'wavy' crack path as observed in experiments.

DOI: 10.1002/nme

3. INTRINSIC *VERSUS* EXTRINSIC COHESIVE ZONE MODELS

Among the various numerical schemes addressing static and dynamic fracture problems, CZMs are of growing interest for fracture modelling and are currently widely used in simulations of both crack growth along predefined path and arbitrary paths. CZM approach is able to simulate fracture processes where cracking occurs spontaneously. The fracture path and speed become natural outcome of the simulation rather than being specified *ad hoc* or *a priori*. In their review paper, Cox *et al.* [1] contend that CZM simulation is particularly promising in investigating certain fracture phenomena including dynamic crack branching.

The concept of 'cohesive failure' is illustrated in Figure 2 for tensile (mode I) case. At the immediate vicinity of crack tip, the material cannot sustain infinitely high stress, and material softens, which results, for example, from void growth and/or microcrack formation [7]. This instance is simulated with the traction–separation relationship law inside the *cohesive zone*, which is along the plane of potential crack propagation. Within the extent of the cohesive zone, the material points which were identical when the material was intact, separate to a distance Δ due to the influence of the stress state at the crack-tip vicinity. The cohesive zone surface sustains a distribution of tractions T which are functions of the displacement jump across the surface Δ, and the relationship between the traction T and separation Δ is defined as the constitutive law for the cohesive zone surface. As an example, in the intrinsic model by Xu and Needleman [18], the constitutive law indicates that with increasing interfacial separation Δ, the traction T across the cohesive interface first increases smoothly, reaches a maximum value at critical separation, then decreases, and finally becomes asymptotically close to zero at a characteristic separation value, where decohesion occurs. The extrinsic model, on the other hand, assumes a monotonically decreasing curve for traction–separation relationship [22].

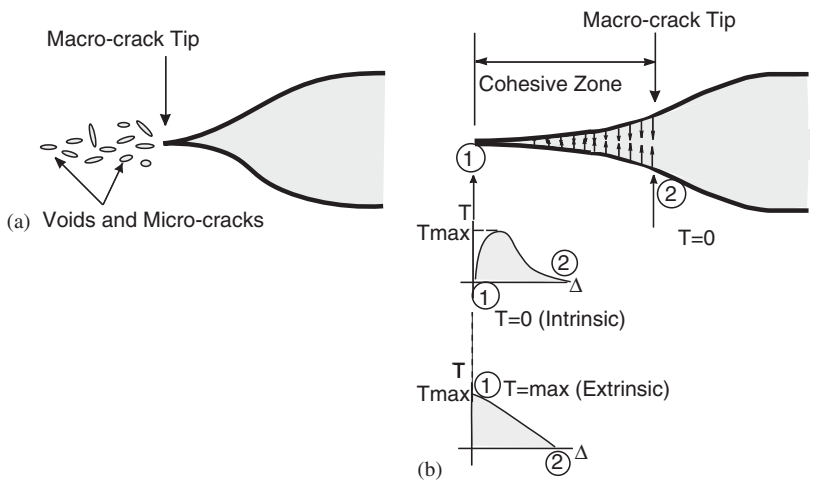

Figure 2. Cohesive zone concept: (a) voids and micro-cracks form in the regions close to the crack tip and (b) CZM considers material softening and separation using distributed cohesive tractions along a cohesive surface at the crack-tip vicinity. Circled numbers ① and ② denote the corresponding positions on the cohesive zone and cohesive law curves where material begins to soften (①) and where material completely loses fracture resistance capacity (②).

DOI: 10.1002/nme

3.1. Historical aspects

Barenblatt [23, 24] and Dugdale [25] first proposed the cohesive zone concept for brittle materials and perfectly plastic materials, respectively. It is postulated that a process zone exists at the crack-tip region, along which a constant cohesive traction (equal to yield strength) closes the material separation. Afterwards, models considering materials with softening behaviour (thus the traction–separation is a decreasing function) were also developed—see [26, 27]. With the development of modern numerical simulation techniques, e.g. FEM, and the availability of large-scale computation, the CZM has been adapted into numerical simulation schemes, and various models have been proposed, e.g. intrinsic CZM with exponential form [18] and bilinear form [28, 29], and extrinsic CZM with monotonically decreasing cohesive strength [30]. These CZMs incorporate a cohesive strength and finite work to fracture in the description of material behaviour, and allow simulation of near-tip behaviour and crack propagation. However, the onset of crack initiation criteria are different for *intrinsic* and *extrinsic* CZMs. The advantages, disadvantages, and limitations of these models were discussed in a few papers—see [18, 28–30]. In general, intrinsic CZMs have been successful in reproducing fracture phenomena when the crack path is pre-defined. For instance, Needleman [31] considered the inclusion debonding case using a potential-based cohesive traction–separation relationship. Tvergaard [32] investigated the fibre debonding problem considering both normal and tangential separations using a CZM without the potential form. The model by Xu and Needleman [18], which incorporates both normal and tangential traction–separation relationships, was widely used later on due to its simplicity and its potential form. The intrinsic CZMs incorporate an initial slope in the traction–separation curve which leads to artificial reduction of stiffness. The other CZM category belongs to the class of extrinsic models, e.g. [22], which eliminate the artificial compliance typical of the intrinsic models mentioned above. Ortiz and co-workers developed models for three-dimensional (3-D) fracture growth and fragmentation simulation [33]. However, depending on implementation, the extrinsic model may lead to time-discontinuous numerical results [34]. There has been discussions and debates over the pros and cons of each model (see Falk *et al.* [35]).

The main distinction between intrinsic and extrinsic CZMs is the presence of the initial elastic curve, as illustrated in Figure 3. Intrinsic CZMs assume that, e.g. in pure tension case, traction T_{n} first increases with increasing interfacial separation Δ_{n}, reaches a maximum value $T_{\mathrm{n}}^{\max}$, then decreases and finally vanishes at a characteristic separation value δ_{n}, where complete decohesion is assumed to occur. On the other hand, extrinsic CZMs assume that separation only initiates when the interfacial traction reaches the finite strength $T_{\mathrm{n}}^{\max}$, at which point the cohesive element is adaptively inserted in the model and nodes are duplicated as required, but there is no physical distance separating these nodes (see Section 5). Once separation occurs, the interfacial cohesion force monotonically decreases as separation increases. Some of these implications are addressed in more detail in the work by the authors [36], where mesh convergence study was carried out for both cracks propagating along a pre-defined path and cracks propagating along an arbitrary path. To characterize fracture processes, the CZM adopted in the present investigation is the one proposed by Ortiz and Pandolfi [33], which is discussed next.

3.2. On Ortiz and Pandolfi's CZM: description and critical assessment

This model eliminates the artificial softening effect due to elastic deformation of cohesive interface present in intrinsic models such as Xu and Needleman's [18]. Ideally, the initial interface stiffness should be infinity, i.e. prior to crack propagation, the cohesive interface should not generate any

DOI: 10.1002/nme

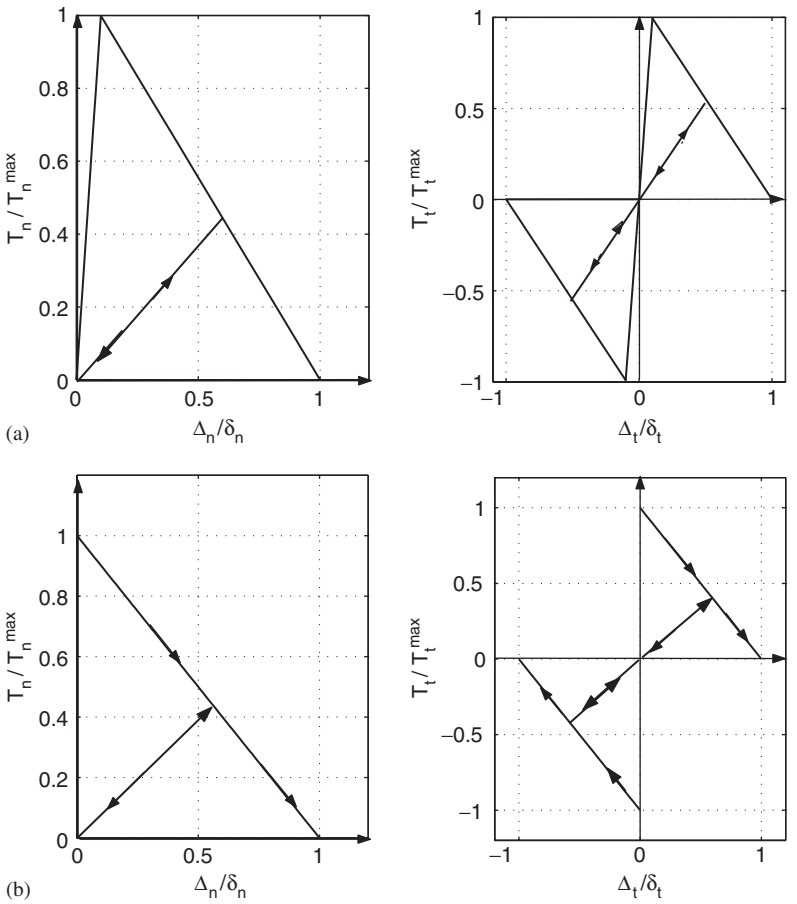

Figure 3. Comparison of two typical intrinsic and extrinsic CZMs: (a) bilinear intrinsic cohesive zone model [28, 29] in pure tension and pure shear and (b) initially rigid extrinsic cohesive zone model [33] in pure tension and pure shear.

deformation. In the implementation stage, the cohesive elements are adaptively inserted into the mesh, i.e. the initial topology of the mesh does not contain any cohesive elements. When a certain fracture criterion is met, a cohesive element is inserted at the proper location of the mesh, which allows the crack to propagate. Since this model requires a fracture criterion which is external to the cohesive law, this kind of CZM is referred to as '*extrinsic*'. The fracture criterion may be chosen in terms of a critical fracture stress T_n^{max} determined from experiments.

This model is based on *effective quantities.* The *effective traction* T_{eff} and *effective displacement* Δ_{eff} are defined as

$$T_{eff} = \sqrt{T_n^2 + \eta^{-2} T_t^2}, \quad \Delta_{eff} = \sqrt{\Delta_n^2 + \eta^2 \Delta_t^2} \quad \text{for } T_n \geqslant 0 \tag{1a}$$

$$T_{eff} = (|T_t|)/\eta, \quad \Delta_{eff} = \eta(|\Delta_t|) \quad \text{for } T_n < 0 \tag{1b}$$

DOI: 10.1002/nme

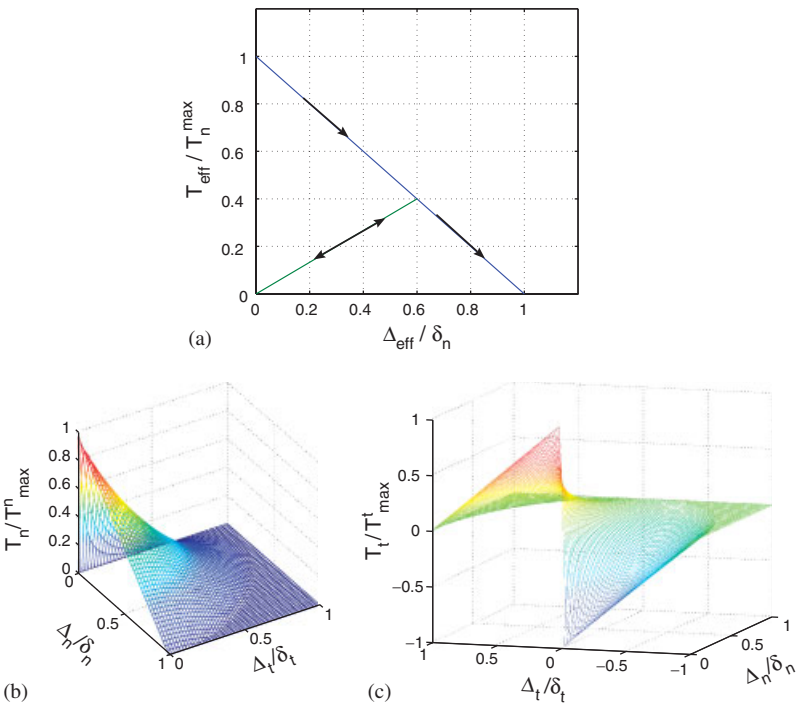

Figure 4. The extrinsic initially rigid cohesive model: (a) relationship between *effective* traction and separation; (b) normalized normal traction T_n/T_n^{max} *versus* normalized opening and sliding separations (Δ_n/δ_n and Δ_t/δ_t); and (c) normalized tangential traction T_t/T_t^{max} *versus* opening and sliding separations. The mode mixity factor is assumed to be $\eta = 1$.

where T_n and T_t are the cohesive tractions in normal and tangential direction, respectively; Δ_n and Δ_t are the opening and sliding separations, respectively; η is the shear stress factor, which represents the mode mixity effect. When the fracture initiation condition

$$T_{eff} \geqslant T_n^{max} \tag{2}$$

is met, a new surface is introduced into the mesh by doubling nodes and creating interface cohesive elements. The cohesive force that resists the opening and sliding of the new surface is assumed to weaken irreversibly with increasing crack opening. Irreversibility is retained by keeping track of the maximum displacement in the simulation history and by using it as the indicator for loading or unloading, as shown in Figure 4(a). The cohesive traction and separation relationship is described next.

Under loading condition, when the current effective opening displacement is larger than that in the history $\Delta_{eff_{(max)}}$, the cohesive traction ramps down linearly as displacement jump increases, and reduces to zero as opening reaches critical opening displacement $\Delta_n = \delta_n$. The decohesion is

DOI: 10.1002/nme

complete at this point and cohesive force vanishes thereafter. Thus,

$$T_{\mathrm{n}} = T_{\mathrm{n}}^{\max}\left(1 - \frac{\Delta_{\mathrm{eff}}}{\delta_{\mathrm{n}}}\right)\frac{\Delta_{\mathrm{n}}}{\Delta_{\mathrm{eff}}}$$
$$T_{\mathrm{t}} = \eta T_{\mathrm{n}}^{\max}\left(1 - \frac{\Delta_{\mathrm{eff}}}{\delta_{\mathrm{n}}}\right)\frac{\Delta_{\mathrm{t}}}{\Delta_{\mathrm{eff}}} \quad \text{for } \Delta_{\mathrm{eff}} \geqslant \Delta_{\mathrm{eff}_{(\max)}} \tag{3}$$

If unloading occurs, the crack begins to close, and the traction obeys the linear unloading relation, assuming unloading towards the origin

$$T_{\mathrm{n}} = T_{\mathrm{n}}^{\max}\left(1 - \frac{\Delta_{\mathrm{eff}_{\max}}}{\delta_{\mathrm{n}}}\right)\frac{\Delta_{\mathrm{n}}}{\Delta_{\mathrm{eff}_{(\max)}}}$$
$$T_{\mathrm{t}} = \eta T_{\mathrm{n}}^{\max}\left(1 - \frac{\Delta_{\mathrm{eff}_{\max}}}{\delta_{\mathrm{n}}}\right)\frac{\Delta_{\mathrm{t}}}{\Delta_{\mathrm{eff}_{(\max)}}} \quad \text{for } \Delta_{\mathrm{eff}} < \Delta_{\mathrm{eff}_{(\max)}} \tag{4}$$

as shown in Figure 4(a). If the crack reopens, the reloading path follows the unloading path in the reverse direction until $\Delta_{\mathrm{eff}_{(\max)}}$ and then follows the original ramp-down relation (3). The traction–separation relationships for normal and tangential cases are illustrated in Figure 4(b) and (c), respectively.

The features of Pandolfi and Ortiz's model [33] are summarized as follows:

- It is an *extrinsic* model, in that the cohesive elements are adaptively inserted into the mesh. Moreover, an extrinsic fracture criterion is required.
- The maximum cohesive strength is usually taken as the tensile strength of material if experimental measurement is available, e.g. [34]. Otherwise it is most often assumed as a fraction of the material stiffness (E), which is much lower than that used in intrinsic models.
- It is based on *effective quantities* as defined in Equation (1), which is unable to consider different fracture toughness in mode-I (G_{I}) and mode-II (G_{II}).
- The relations between normal and tangential components of the traction and separation are not coupled. Effect of mode mixity is represented by the arbitrary parameter η, whose value can vary within a large range, e.g. $\eta = 0.1$ in Reference [37], $\eta = 0.707$ in Reference [33], and $\eta = 2.3$ in Reference [34].

4. NUMERICAL SCHEME

To incorporate a CZM into the numerical scheme for dynamic fracture simulation, the *cohesive element* is developed and implemented as part of the finite element scheme, which follows a cohesive *traction–separation* relationship. In contrast, the conventional volumetric finite element, which is now called '*bulk* element', follows conventional *stress–strain* relationships (continuum description).

4.1. Finite element scheme incorporating cohesive elements

Figure 5 illustrates the concept of the two classes of elements mentioned above: bulk and cohesive. The bulk behaviour of the material is accounted for by conventional volumetric elements, whose constitutive relationship is defined, for example, by Hooke's Law. To model fracture initiation and

DOI: 10.1002/nme

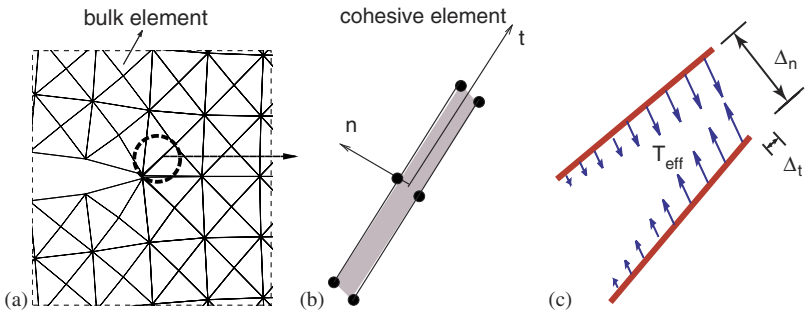

Figure 5. Schematic representation of *bulk* elements and *cohesive* elements in the finite element formulation. The notations are as follows: T_{eff} denotes effective traction, Δ_n, Δ_t denote separation along normal and tangential direction, respectively: (a) a discretized region with a cohesive element inserted along the circled edge; (b) orientation of cohesive element; and (c) traction follows the extrinsic cohesive zone model shown in Section 3.2.

propagation, cohesive elements are inserted 'on-the-fly' to the existing mesh, positioned along the predicted crack path, and attached to the bulk elements. Once inserted, the cohesive elements produce cohesive traction that resists opening, depending on the interface separation by the cohesive law. When interface opening exceeds critical value, the element loses all capacity against separation and crack advances. The constitutive law of cohesive elements is inherently embedded in the finite element model, so that the presence of cohesive elements allows spontaneous crack propagation, and thus it is very promising in the investigation of bifurcation and/or of impact dynamic loading, where multiple crack paths are possible. The difficulty of employing extrinsic cohesive model in finite element method, however, resides in the extensive updating of mesh and topological information as crack advances, which is discussed in Section 5.

4.2. Principle of virtual work

The FEM formulation with cohesive elements can be derived from the principle of virtual work, as described below. The principle of virtual work of the dynamic finite element formulation can be expressed as [18]

$$\int_{\Omega} (\operatorname{div} \boldsymbol{\sigma} - \rho \ddot{\mathbf{u}}) \delta \mathbf{u} \, \mathrm{d}\Omega - \int_{\Gamma} (\mathbf{T} - \boldsymbol{\sigma}\mathbf{n}) \delta \mathbf{u} \, \mathrm{d}\Gamma = 0 \tag{5}$$

where Ω represents domain area (or volume), Γ denotes boundary line (or surface) with normal vector $\mathbf{n}$, $\mathbf{u}$ is the displacement vector, $\mathbf{T}$ is the traction on the boundary, and $\boldsymbol{\sigma}$ is the Cauchy stress tensor. The superposed dots in $\ddot{\mathbf{u}}$ denote differentiation with respect to time ($\ddot{\mathbf{u}} = \partial^2 \mathbf{u}/\partial t^2$), and ρ is the material density. Considering the existence of cohesive surface, applying the divergence theorem and integrating by parts the general expression in (5), one obtains the following expression:

$$\int_{\Omega} (\boldsymbol{\sigma} : \delta \mathbf{E} + \rho \ddot{\mathbf{u}} \cdot \delta \mathbf{u}) \, \mathrm{d}\Omega - \int_{\Gamma_{\text{ext}}} \mathbf{T}_{\text{ext}} \cdot \delta \mathbf{u} \, \mathrm{d}\Gamma - \int_{\Gamma_{\text{coh}}} \mathbf{T}_{\text{coh}} \cdot \delta \Delta \mathbf{u} \, \mathrm{d}\Gamma = 0 \tag{6}$$

where Γ_{ext} represents the boundary line on which external traction $\mathbf{T}_{\text{ext}}$ is applied, and $\mathbf{E}$ is the Green strain tensor. The contribution of cohesive traction–separation work is accounted by the last

DOI: 10.1002/nme

term integrating over the internal cohesive surfaces Γ_{coh} on which the cohesive tractions $\mathbf{T}_{\text{coh}}$ and displacement jumps $\Delta\mathbf{u}$ are present. In the context of extrinsic cohesive modelling, the cohesive surface Γ_{coh} is not a constant, but varies over time as cohesive elements are adaptively inserted in the model.

The integrals in Equations (5)–(6) are carried out in the deformed configuration. When the expression is cast into the undeformed configuration, work conjugates other than $\boldsymbol{\sigma}$ and $\mathbf{E}$ are used. With all quantities referred to as undeformed configuration, the following expression is obtained instead:

$$\int_{\Omega} (\mathbf{S} : \delta\mathbf{E} + \rho\ddot{\mathbf{u}} \cdot \delta\mathbf{u})\, \mathrm{d}\Omega - \int_{\Gamma_{\text{ext}}} \mathbf{T}_{\text{ext}} \cdot \delta\mathbf{u}\, \mathrm{d}\Gamma - \int_{\Gamma_{\text{coh}}} \mathbf{T}_{\text{coh}} \cdot \delta\Delta\mathbf{u}\, \mathrm{d}\Gamma = 0 \tag{7}$$

where $\mathbf{S}$ denotes the second Piola–Kirchhoff stress tensor, which is related to the Cauchy stress tensor $\boldsymbol{\sigma}$ as follows (e.g. Belytschko *et al.* [38])

$$\mathbf{S} = J\mathbf{F}^{-1}\boldsymbol{\sigma}\mathbf{F}^{-\mathrm{T}} \quad \text{where } J = \det\mathbf{F} \tag{8}$$

and $\mathbf{F}$ denotes the deformation gradient tensor. This formulation is used in the current study.

In the present work, the explicit central difference time stepping scheme (see, Bathe [39]; and Belytschko *et al.* [40]) is used, according to the updating scheme described by Zhang and Paulino [36]. The main difference with respect to the standard central difference method is the introduction of the cohesive force vector in the formulation.

5. FRAMEWORK USING THE TOPOLOGICAL DATA STRUCTURE (TopS)

Extrinsic CZMs require modifications of the mesh during the course of the simulation for the adaptive insertion of new cohesive elements along bulk element interfaces. In order to efficiently handle such modifications, the mesh has to be described by means of a topological data structure, thus acquiring efficient access to the topological adjacency relationships among the defined topological entities. In this work, the adjacency-based TopS presented in our previous work [9] is used. TopS is a topological data structure for finite (or boundary) element representation. It provides the necessary framework for applications that need efficient access to topological information relating the entities that compose the mesh, for both 2-D and 3-D models. TopS is especially designed to support adaptive analysis, such as dynamic crack propagation. It is a compact and complete topological data structure [9]. The compactness of the data structure is important for not imposing a prohibitive cost in memory space to represent large models. The completeness of the data structure is crucial in order to have efficient access to all adjacency relationships among the topological entities that compose the model (which is needed, for instance, to insert interface element along facets of bulk elements during the course of a fragmentation simulation). In this work, the data structure was used to support 2-D models, but it was designed to support both 2-D and 3-D models with any type of element defined by templates of ordered nodes, including all Lagrangian-type elements and their corresponding cohesive elements. The data structure was designed for *manifold* mesh domains. This means that the external boundary of a 2-D mesh must have 1-manifold topology; therefore, each vertex on the boundary is shared by exactly two boundary edges. Such restriction on the domain boundary does not impose any limit to the support of fragmentation simulation, because the insertion of cohesive elements preserves the domain's manifoldness.

DOI: 10.1002/nme

5.1. Topological framework for cohesive element insertion

In TopS, the model represents the 'mesh' as a whole. The application can load and manipulate a set of models at a given time, but the models are independent; i.e. there is no relationship among different models. Each model is described by means of topological entities. Actually, TopS defines five topological entities, which are:

- *Element*: The topological entity element represents a finite (or boundary) element of the mesh. There are different types of elements. Each finite element type (T3, Q4, T6, etc.) is represented by a different type of topological element, and a model can be described by sets of different types of elements. For instance, in a model for fragmentation simulation, the mesh is composed at least by two different types of element: bulk and cohesive elements.
- *Node*: The topological entity node represents a node of the mesh. Both corner and mid-side nodes, for non-linear mesh, are represented by the same topological entity in TopS. Once a node is accessed, one can query the data structure if it represents a corner or a mid-side node, but both types are mapped to the same topological entity.
- *Facet*: The topological entity facet represents the interface between two elements. In 2-D models, it is mapped to a 1-D entity; in 3-D models, it is mapped to a 2-D entity.
- *Edge*: The topological entity edge delimits a facet. It corresponds to a 1-D entity. For 2-D models, each edge corresponds to a facet, and *vice versa*. However, to keep the use of the data structure consistent for both 2-D and 3-D models, one should opt for referencing a facet whenever it is desired to have access to the interface between two elements. For instance, in a fragmentation simulation, the topological entity facet is the right place to store fracture properties.
- *Vertex*: The topological entity node represents the boundary of an edge. There is a vertex associated to each corner node; no vertex is associated to a mid-side node.

Internally, TopS only explicitly represents *element*, and *node*. All other topological entities (facet, edge, and vertex) are implicitly represented. This means that, although they exist and can be accessed, there is no memory cost associated with them. For the client application point of view, it does not matter the way a topological entity is internally represented: the application is allowed to freely list, access, attach properties to, and hold references to any entity in a transparent way, despite it being explicitly or implicitly represented. For instance, it is a valid operation to visit all the edges of the model. For each visited edge, TopS returns to the client application a value representing the corresponding edge. The client can use such a value (the edge) to query the data structure, to attach attribute to it, and so on. No memory allocation is performed for visiting the edges; this operation is as efficient as visiting the set of elements, which are explicitly represented.

Facet, edge, and vertex are called non-oriented entities because there is no orientation associated to them. TopS also introduces three oriented entities, which are:

- *Facet-use*: The topological entity *facet-use* represents the use of a facet by an element. Each facet has two associated facet-uses, corresponding to the two interfacing elements (except the external facets that have only one associated facet-use, since they represent the mesh boundary).
- *Edge-use*: The topological entity *edge-use* represents the use of an edge by an element. For 2-D models, each edge has two associated edge-uses. For 3-D models, each edge has a radially ordered set of associated edge-uses.

DOI: 10.1002/nme

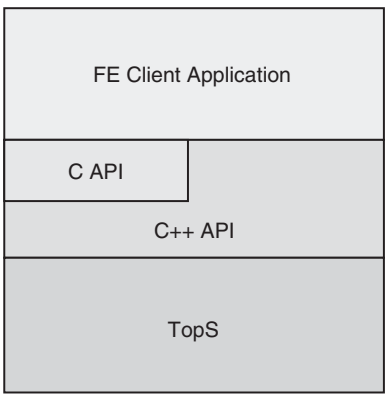

Figure 6. Schematic representation of C + + and C application programming interface between FE application and TopS data structure.

- *Vertex-use*: The topological entity *vertex-use* represents the use of a vertex by an element. For 2-D models, each vertex has a cyclically ordered set of associated vertex-uses. For 3-D models, each vertex has an unordered set of associated vertex-uses.

For 2-D models, a facet corresponds to an edge, and *vice versa*. Such redundancy does not impose any additional memory cost because the entities are implicitly represented. Moreover, defining both facet and edge as distinct topological entities has resulted in a unified framework for 2-D and 3-D models. In fact, TopS provides support for the insertion of cohesive elements along any facet that represents the interface between two bulk elements. The insertion of a cohesive element may require the duplication of nodes, thus changing the connectivity of neighbouring elements. Whether a node has to be duplicated or not depends on the topological classification of the fractured facet. All mesh modifications due to the insertion of a new cohesive element are based on local topological operations, thus being performed very efficiently: the time needed to insert a new cohesive element is proportional to the number of topological entities adjacent to the fractured facet [9].

The finite element (FE) analysis code interacts with the TopS through either a C or a C + + application-programming interface (API), as shown in Figure 6. The interface is designed to provide the users with a unified and transparent access to the data structure. Both C API and C + + API provide a broad range of capabilities and direct access to the underlying topological entities. In this work, we used the C API, accessing functions to

- Set up the initial mesh composed uniquely by bulk elements, inserting the nodes and the bulk elements in the data structure.
- Attach application attributes to the topological entities, traversing the entities and computing initial attributes to be attached. Such attributes are later retrieved and modified during the course of the simulation.
- Insert cohesive elements, identifying fractured facets and asking the data structure to insert the cohesive elements along such facets. The data structure automatically adjusts the mesh, performing all needed topological modifications.

DOI: 10.1002/nme

5.2. Criteria for adaptive insertion of cohesive elements

TopS is a modular computational layer which can be interfaced with any analysis code. In the present work, the insertion of new cohesive elements along the interfaces between bulk elements is performed by the following procedure at chosen time intervals:

- *Calculate the stress at each interfacial Gauss point*: For each facet between two bulk elements in the entire domain, convert the stress components to normal and tangential tractions along the facet given by the outer normal, which are used to computer the effective traction T_{eff}.
- *Flag fractured facets*: When criterion $T_{\text{eff}} \geqslant T_{\text{n}}^{\max}$ is satisfied, the facet is flagged to be the site of cohesive element insertion.
- *Insert cohesive elements*: Call the TopS functions to insert new cohesive elements along fractured facets, updating the attributes of elements and nodes.
- *Compute initial traction*: For newly inserted cohesive elements, compute initial traction at each Gauss point along the interface and scale the effective traction to $T_{\text{n}}^{\max}$ (according to the traction–separation curve). At the instance of cohesive element insertion, both the normal and tangential separations are zero.

5.3. Topological operations to insert cohesive elements

Once identified the facet along which a new cohesive element has to be inserted, the data structure performs a set of topological operations in order to update the mesh. Considering a triangular mesh, the set of operations is given by:

- *Classify the facet against the mesh boundary*: For each bounding vertex of the edge associated to the fractured facet, the data structure checks whether it lays on the mesh boundary. This checking is done by retrieving all the adjacent facets around the vertex and verifying if any of them represents the interface between a bulk element and the external boundary or between a bulk element and an existing cohesive element.
- *Duplicate the mid-side nodes*: For quadratic (or higher-order) elements, duplicate the mid-side nodes along the edge associated to the fractured facet.
- *Duplicate the corner nodes*, *if necessary*: For each vertex on the boundary, duplicate the associated element-corner node.
- *Update the element incidences*: For each duplicated node, update the incidence of adjacent elements. The data structure identifies which elements must have their incidence updated.
- *Insert a new cohesive element in the model*: Insert a new cohesive element with incidence given by the new set of nodes along the fractured facet.

Figure 7 shows a schematic example of crack propagation resulting in a simple branching pattern. For each time step, the fractured facet is classified and the corresponding nodes are duplicated according to such classification. The figure illustrates part of a triangular mesh with T6 elements (for clarity, the mid-side nodes are not shown). In this example, at the first time step (Figure 7(a)), the crack tip is at node A. In a next time step, the facet associated to edge AB fractures, requiring the insertion of a new cohesive element. As, at this point, the vertex associated to node A is on the boundary and the vertex associated to node B is not on the boundary, node A, together with the mid-side node, is duplicated (Figure 7(b)). At the following time step, a bifurcation occurs and both facets associated to edges BC and BD fracture. Considering that the facet associated to BC is checked first, node B is duplicated but node C is not (Figure 7(c)). After the duplication of

DOI: 10.1002/nme

node B, the facet that was associated to BD becomes associated to B′D. It is then checked and node B′ is duplicated, but node D is not (Figure 7(d)). Finally, in the last illustrated time step, the facets associated to edges CE and DF are checked. In both cases, the two end nodes, C, E and D, F, are duplicated because all of them are on the current mesh boundary (Figures 7(e) and (f)).

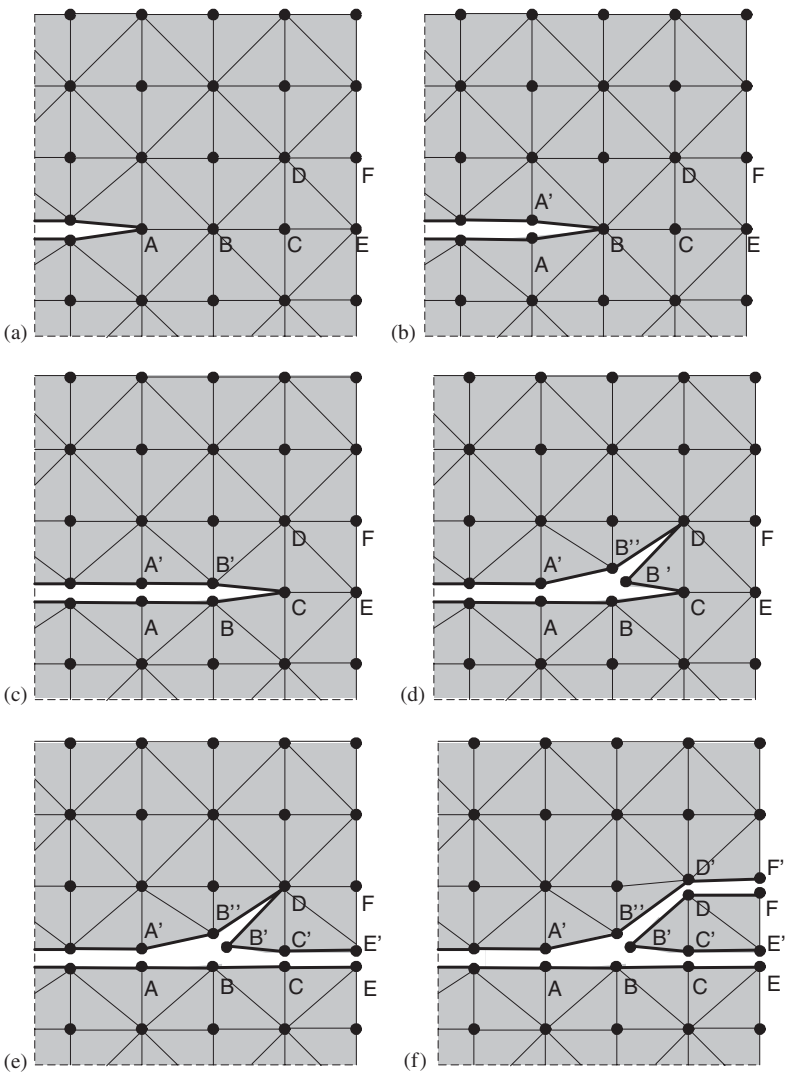

Figure 7. Insertion of cohesive elements along crack propagation with a simple branching pattern: (a) crack tip at node A; (b) fracture of facet AB with node A being duplicated; (c) fracture of facet BC with node B being duplicated; (d) fracture of facet B'D with node B' being duplicated; (e) fracture of facet CE with both nodes C and E being duplicated; and (f) fracture of facet DF with both nodes D and F being duplicated.

DOI: 10.1002/nme

6. SIMULATION OF MICROBRANCHING INSTABILITY EXPERIMENT

In this section, the crack propagation in a pre-stretched narrow strip is investigated for PMMA material. The prescribed geometry and boundary conditions result in the so-called 'quasi-steady-state crack propagation' [41] problem, i.e. the crack runs at a relatively constant speed throughout the strip. Because consideration of the actual specimen size would require computations exceeding our available computational resources, this study instead uses a geometry of reduced dimension in comparison with the original experiment, while keeping the specimen aspect ratio and unit energy supply the same as the experiment. A similar reduced-order model was also employed by Miller *et al.* [42]. Simulation results indicate that most of the features of the experiment are well reproduced. First, the mesh convergence of the numerical method is investigated. Results of the crack-tip velocity suggest that the criterion for mesh size *versus* crack-tip process zone size depends upon not only the material property but also the boundary conditions. Next, the relationship between fracture behaviour and applied load is analysed and compared with experimental observations. Finally, energy balance is investigated in detail, which also provides verification of the numerical implementation.

6.1. Problem description

Sharon and his co-workers [6, 41, 43] investigated 'quasi-steady-state crack propagation', focusing on characterization of the relationship between microcrack pattern, crack surface characteristics and crack speed. The experimental setting is schematically shown in Figure 8. The upper and lower boundaries are clamped, and uniform stress of magnitude of $\sigma = 10$–18 MPa is applied. Afterwards, the boundaries are held fixed, and a sharp crack is introduced along the blunt pre-notch using a razor blade. The energy stored in the system thus spurs crack propagation through the strip.

Since the cohesive model approach requires fine mesh size to capture the non-linear behaviour at the crack-tip region, the original experiment size is reduced in proportion in the numerical analysis. Figure 9 shows the geometry and boundary conditions used in the study.

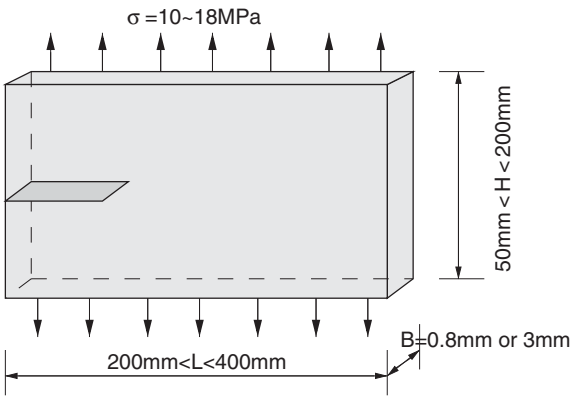

Figure 8. Model of the experimental setting by Sharon and Fineberg [6]; the length to height ratio $(L : H)$ is kept from 2 to 4, in order to represent steady-state crack propagation condition.

DOI: 10.1002/nme

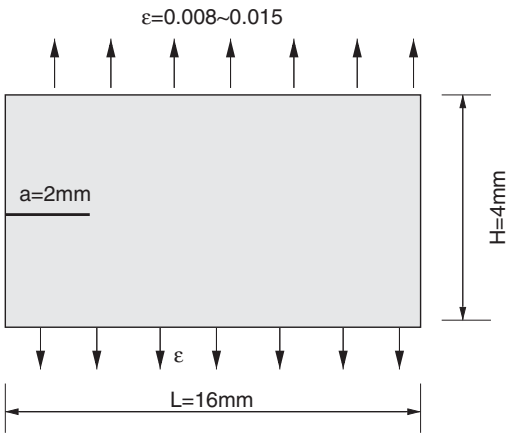

Figure 9. Schematic representation of the geometry and boundary condition for the 2-D steady-state crack propagation problem, using reduced dimension based on Sharon and Fineberg [6]; the length to height ratio $(L:H)$ is 4.

Table I. Properties of PMMA [18] strip subjected to initial stretch.

E (GPa)	v	ρ (kg/m^3)	G_{Ic} (N/m)	$T_{\mathrm{n}}^{\max} = T_{\mathrm{t}}^{\max}$ (MPa)	$\delta_{\mathrm{n}} = \delta_{\mathrm{t}}$ (μm)	η	c_{R} (m/s)
3.24	0.35	1190	352.3	129.6	5.44	1	939

The strip is initially stretched uniformly by imposing an initial displacement field

$$u(x, y; t = 0) = 0, \quad v(x, y; t = 0) = \varepsilon y \tag{9}$$

which results in a uniform strain field (ε) at the initial time. The upper and lower surfaces are held fixed and a small crack length a is introduced at the left edge at time $t = 0$. The material used is PMMA [18], and its properties are given in Table I. In the numerical simulations G_{IIc} is assumed to be equal to G_{Ic} ($G_{\mathrm{IIc}} = G_{\mathrm{Ic}}$).

6.2. Reduced dimension model

The cohesive model approach demands a suitably refined mesh around the crack-tip region such that the non-linear behaviour at the crack-tip vicinity can be properly simulated by the cohesive elements. Since the present problem involves numerous branchings without pre-defined paths across the entire strip, the strip is meshed with very fine elements. Moreover, small element size ensues small time step required by explicit updating scheme. As a consequence, the numerical simulation becomes enormously heavy if the original experimental model is used, which results in a FEM consisting of 20 million nodes and 10 million bulk elements when the fine mesh discretization is used. Such large-scale computation is better suited for super-computers, which were not available for the present study. Therefore, in order to achieve a numerical study that reasonably represents the original problem while keeping the computation overhead under control, the reduced model in Figure 9 is adopted in the study, which is the same model dimension used by Miller *et al.* [42]. This approach introduces size effect considerations beyond what has been addressed in this work.

DOI: 10.1002/nme

For further information on size effect and scaling, the reader is referred to the work by Bažant and Planas [27].

Material properties listed in Table I follow those of Miller *et al.* [42], except for cohesive strength $T_{\mathrm{n}}^{\max}$ and characteristic separation δ_{n}. Miller *et al.*'s work [42] uses an exponential-form intrinsic cohesive model which assumes a high cohesive strength (1/10 of Young's modulus for PMMA). Adoption of the high value is motivated more by trying to control the artificial compliance, which is unavoidably associated with the intrinsic model, rather than experimental evidence. Admittedly, cohesive strength can rarely be obtained from experiments with high reliability [19], yet the available reported tensile strength of PMMA (62.1 MPa) is much lower than that used by Miller *et al.* [42] (324 MPa). The mode-mixity factor is taken as $\eta = 1$ (cf. Equation (1a)).

The selection of cohesive strength in the present study is related to the reduced dimension problem, which does not represent the original experiment completely because of the material-dependent length scales. *The modelling guideline consists of maintaining the same amount of strain energy per unit length along the strip for the original experiment and the reduced dimension problem*. This consideration results in the increasing of applied loading compared to the experiment. In the experiment, the initial load results in an amount of stored strain energy per unit length of approximately 800–5000 $\mathrm{Nm/m^2}$ [6], and a stretch of approximately $\varepsilon = 0.0027$–0.0049 along the vertical direction at initial time. To maintain the same energy stored per unit length in the numerical analysis as in the experiment, the stress and strain applied at the initial time are much higher in the former case (numerics) than the latter (experiments). The applied load in the experiment (10–18 MPa) is much lower than material tensile strength (62.1 MPa), while in numerical analyses the initial uniform stress (37 to 96 MPa) is close or even higher than material tensile strength. As a consequence, if the material tensile strength is chosen as the cohesive strength, numerous interfaces will break at the initial loading, which is confirmed by the authors' numerical study (results not reported here). Therefore, to avoid unwanted fracture at locations without stress concentration, the cohesive strength used in the present study ($E/25 = 129.6$ MPa) is chosen to be higher than the boundary loading. This value does not match the real material tensile strength (62.1 MPa), and the difference between the actual and reduced dimension must be considered in interpreting the numerical results.

6.3. Mesh convergence

The domain is uniformly discretized by T6 elements of various element sizes as shown in Figure 10 and Table II. Time step Δt is chosen as a fraction (around 10%) of that required by the Courant condition for explicit updating scheme, to ensure stable computation when cohesive elements are present. Cohesive elements are adaptively inserted in the FE mesh, which allow crack to spontaneously grow and branch.

Driven by the strain energy stored in the pre-stretched strip, the crack propagates towards the right edge of the strip. When the mean effective traction obtained from averaging the tractions at three nodes meet the fracture criterion (Equation (2)), cohesive element is inserted adaptively. In actual experiments, unless the crack path is constrained, the crack-tip speed can hardly reach 50% of the Rayleigh wave speed due to energy dissipation mechanisms, for example, from micro-crack formation at the immediate crack-tip vicinity. The energy dissipation mechanism is simulated by the formation of microbranching at crack tip.

Various mesh discretizations are employed to investigate the convergence of the numerical scheme in terms of the relationship between the characteristic cohesive length scale δ and mesh

DOI: 10.1002/nme

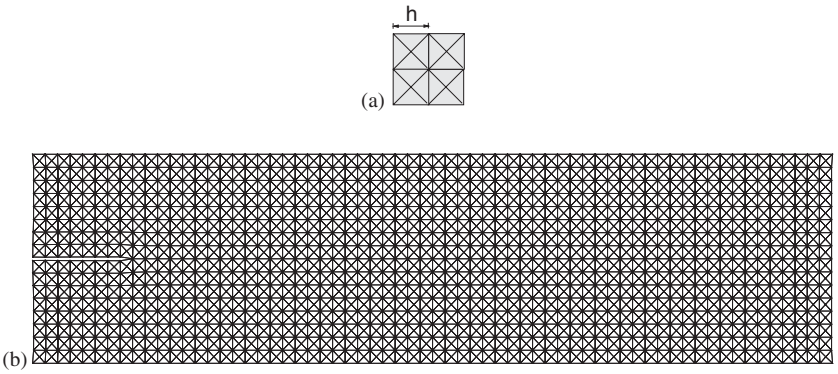

Figure 10. Mesh discretization with T6 elements for pre-cracked PMMA strip subjected to initial stretch: (a) mesh pattern and characteristic length h, which is defined as grid spacing and (b) mesh with grid 16×64, $h = 250$ μm. Other meshes with grid 32×128 ($h = 125$ μm), grid 48×192 ($h = 83$ μm) and grid 64×256 ($h = 62.5$ μm) use the same mesh pattern with different levels of refinement.

Table II. Mesh discretization and time step control associated with Figure 10.

Mesh	Grid	h (μm)	ℓ_{cz}/h	# Nodes at $t = 0$	# Bulk elements	Δt (μs)
(1)	16×64	250	0.5	8369	4096	8×10^{-3}
(2)	32×128	125	1.0	33 121	16 384	4×10^{-3}
(3)	48×192	83	1.5	74 257	36 864	3×10^{-3}
(4)	64×256	62.5	2.0	131 777	65 536	2×10^{-3}

size h. Here, h is defined as the grid spacing (see Figure 10). Previous researchers who have used intrinsic cohesive models [19, 28] recommend that at least two to three cohesive elements be present inside the cohesive zone, whose size is estimated by [44]

$$\ell_{cz} = \frac{\pi}{8} \frac{E}{1 - \nu^2} \frac{G_{Ic}}{\sigma_{\text{ave}}^2} \tag{10}$$

where for the cohesive law employed, $\sigma_{\text{ave}} = 0.5 T_{\text{n}}^{\max}$. For the material property chosen (Table I), the estimated cohesive zone size is $\ell_{cz} = 122$ μm. However, this estimate originated from a *static* problem [44]. In a previous study by the authors [36], numerical simulation results for crack propagation along pre-defined path also reveal that mesh convergence is achieved at different levels of mesh refinement for different loading conditions, although the cohesive element properties are identical. The issue of dynamic cohesive zone size certainly merits further investigation for dynamic problems with rate effects, however, it is not pursued in the present study. An intrinsic time scale implied in the cohesive model was discussed in a series of papers by Ortiz and his co-workers [22, 45, 46]. This *characteristic time* is defined as

$$t_{\text{c}} = \frac{\rho c_{\text{d}} \delta_{\text{n}}}{2 T_{\text{n}}^{\max}} \tag{11}$$

DOI: 10.1002/nme

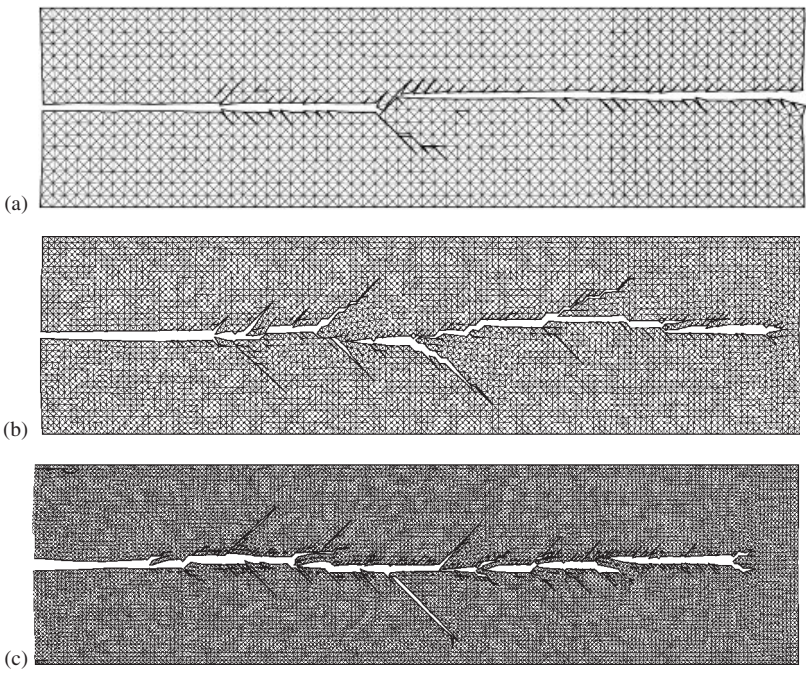

Figure 11. Mesh size influence on fracture pattern for applied stretch $\varepsilon = 0.015$: (a) 16×64 grid, simulation time $t = 24$ μs; (b) 32×128 grid, simulation time $t = 22$ μs; and (c) 48×192 grid, simulation time $t = 21$ μs. Note that the crack branches arrest, as in the experiments by Sharon and Fineberg [6].

where ρ and c_d denote mass density and dilatational wave speed, respectively. Pandolfi *et al.* [45] indicated that the characteristic time influences crack initiation and propagation. Moreover, we also observe that the characteristic time scale influences minimum time step Δt required for convergent numerical result. For higher cohesive strength $T_n^{\max}$ (thus smaller critical opening), characteristic time is lower, and so is time step Δt. The characteristic time scale for the cohesive law employed is $t_c = 0.052$ μs, while $\Delta t = 0.002$–0.008 μs for the computation (Table II), which is about one order lower than the characteristic time.

The influence of mesh size on the evolution of the crack propagation pattern is shown in Figure 11 for an initial stretching parameter $\varepsilon = 0.015$. Evidently, the fracture and branching patterns are influenced by mesh refinement. The numerical result for coarse mesh (Figure 11(a)) indicates few major branching. A close study reveals that minor branching do occur at almost every element intervals as the main crack advances, however, the majority of these branches close afterwards, except for a few. For more refined meshes, Figures 11(b) and (c) reveals similar fracture patterns both in branching angle and major branching spacing. Minor branches emanate from the main crack every couple of elements in a random pattern, and then arrest after running one or at most a few elements length. On the other hand, major (longer) branches appear between a certain distance, growing alternatively on each side of the main crack. These major microbranches extend about 0.5–1 mm and then arrest. This pattern is similar in both Figures 11(b) and (c). The present computational framework clearly demonstrates that the crack branches arrest, as shown in the

DOI: 10.1002/nme

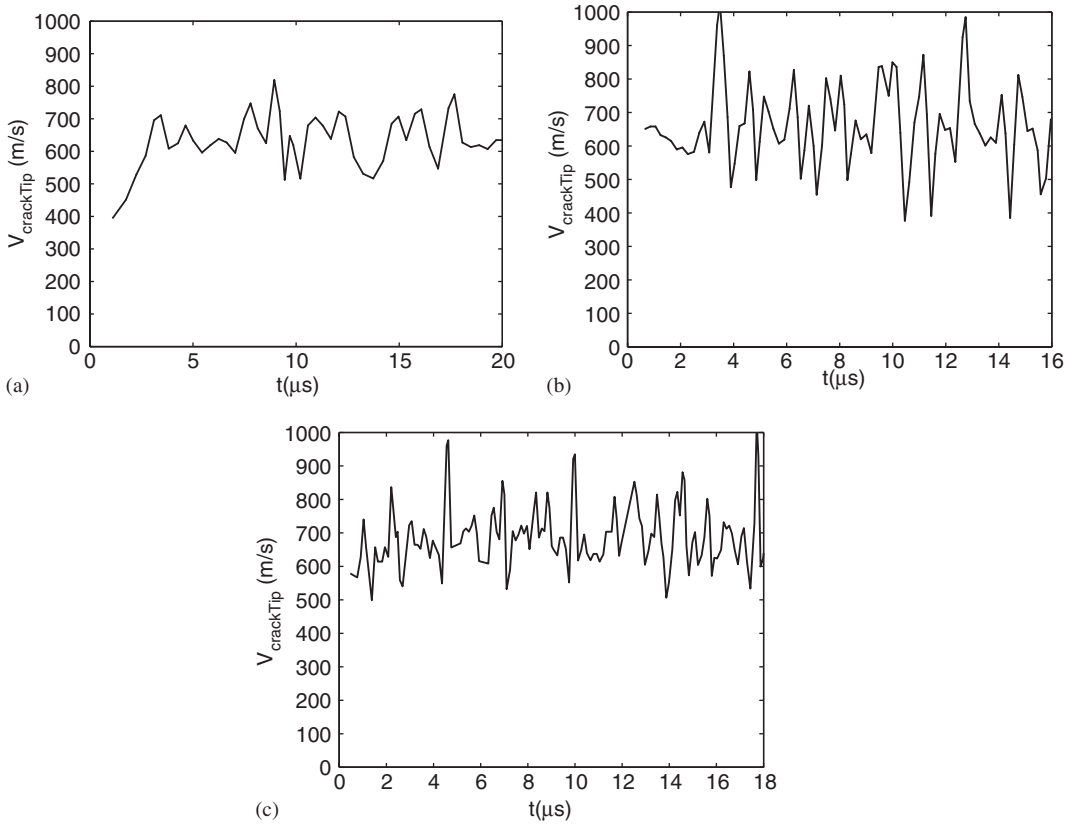

Figure 12. Crack velocity *versus* time considering initial stretch $\varepsilon = 0.015$ and various levels of mesh refinement: (a) grid 16×64; (b) grid 32×128; and (c) grid 48×192.

experiments by Sharon and Fineberg [6]. In contrast, the crack branches do not get arrested in the work by Miller *et al.* [42] (see Figure 7).

The influence of mesh size on crack propagation velocity is shown in Figure 12. Since there is usually more than one crack (including major and minor branches) during the simulation time, the velocity reported in Figures 12 and 14(c) is for the main crack, which is associated with the currently most advanced crack tip but excluding those side branches. Calculation of the crack velocity follows that described in [18]. A quadratic polynomial is fit through three points of the crack length (a) *versus* time (t) curve, say a_{n-1}, a_n and a_{n+1}, and the slope of this quadratic curve at t_n is taken as the crack speed V_n at t_n. Oscillation pattern is observed in all three mesh cases, which is accompanied by the occurrence of microbranching. When a new microbranch appears, velocity for the main crack drops as energy released from stored strain energy in the strip flows into more channels. As the main crack advances and the microbranch closes at its trail, more energy flows back to the main crack and it accelerates. Depending on the frequency of microbranch occurrence and the length each microbranch runs, oscillation pattern appears repeatedly throughout the simulation. For refined mesh, more microbranches occur with sharper fluctuation in the velocity

DOI: 10.1002/nme

Table III. Crack initiation time and average crack speed for loading case $\varepsilon = 0.015$ using different mesh discretizations.

Mesh	Grid	h (μm)	Crack initiation time (μs)	Average crack velocity (m/s)
(1)	16×64	250	1.12	633
(2)	32×128	125	0.67	642
(3)	48×192	83	0.47	642

history (Figure 12). However, the main crack velocity oscillates along an 'average' value, which is roughly the same for different meshes (633, 642 and 642 m/s for the three meshes). Table III compares the initial crack propagation time and average crack speed for different mesh sizes for the same problem. For refined mesh, crack initiation occurs relatively earlier (Table III). Note that for the specific applied load, the results are meaningful and consistent despite the fact that the mesh sizes used do not strictly satisfy the recommended relationship between mesh size and statically estimated cohesive zone size [19, 28] mentioned above. Again, such estimated cohesive zone size provides merely a guidance in dynamic fracture problems. A previous investigation for mesh convergence involving a single crack propagation problem [47] also suggested that this requirement is problem dependent and can be relaxed under certain conditions.

Similar investigations are carried out for various initial stretches, which indicate that mesh size criterion is more stringent for problems of lower stretch loading. For example, for initial stretch $\varepsilon = 0.012$ as shown in Figure 13, the coarse mesh (16×64 grid, Figure 13(a)) is not sufficient to initiate crack propagation, while for subsequently refined mesh, results of similar trend are obtained. Microbranching pattern for 48×192 grid mesh (Figure 13(c)) is slightly different: a major bifurcation occurs at about 1/3 of the strip length and the upper branch dominates later while the lower one closes after extending for about 3 mm. However, the overall branching pattern, in terms of microbranch extension length and interval, as well as average crack propagation speed, is similar to the other two meshes (32×128 grid and 64×256 grid, Figures 13(b) and (d)).

For initial stretch $\varepsilon = 0.01$, the coarse mesh is not sufficient to initiate crack propagation, as shown in Figure 14(a). With refined mesh, crack propagates at an average speed of around 572 m/s through the strip (Figures 14(b) and (c)).

6.4. Influence of applied load on microbranch patterns

Experiments [6] indicate that with increasing stored energy, the crack runs at higher velocity and generates longer and more noticeable microbranches. Figure 15 demonstrates the transition from smooth crack to more roughened crack with significant microbranches as initial stretch increases. The branches plotted in the figure consist of all the completely separated cohesive surfaces. The condition for cohesive element failure is defined such that all three Gauss points of the elements have experienced complete decohesion (in terms of separation Δ_{eff}). Therefore, some cohesive surfaces that are still active (i.e. not all Gauss points have reported decohesion), are not included. Consequently, a 'smooth' crack in the plot does not indicate non-existence of any microbranch, rather, it means that even though microbranch may occur, they arrest before running more than one element length. With this understanding, Figure 15(a) indicates that for $\varepsilon = 0.0085$ case, the main crack runs smoothly through the entire strip, while more microbranches appear for $\varepsilon = 0.009$ and 0.01 cases (Figures 15(b) and (c), respectively). As applied loading increases, the microbranches

DOI: 10.1002/nme

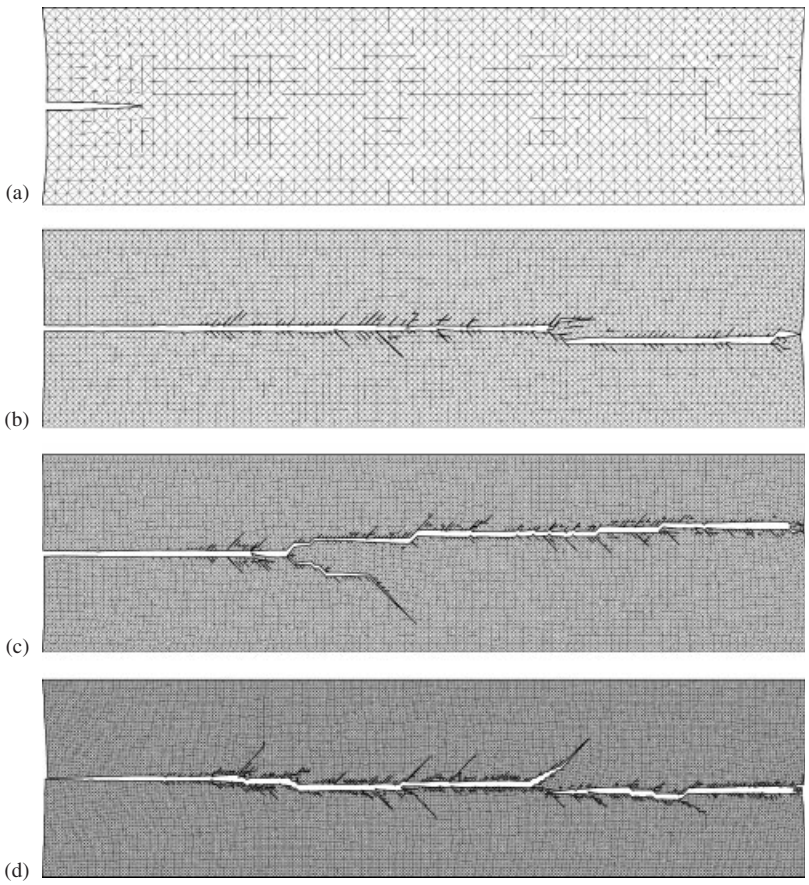

Figure 13. Mesh size influence on fracture pattern for applied stretch $\varepsilon = 0.012$: (a) 16×64 grid, simulation time $t = 32$ μs; (b) 32×128 grid, simulation time $t = 24$ μs; (c) 48×192 grid, simulation time $t = 24$ μs; and (d) 64×256 grid, simulation time $t = 23.4$ μs.

also extend longer, as shown in Figure 15(d). This overall trends are in agreement with the experiments by Sharon and Fineberg [6].

6.5. Influence of applied load on crack velocity

Comparison of crack initiation time and average crack speed for the simulations in Figure 15 is provided in Table IV. To avoid boundary effect influence on the calculated velocity result, average velocity is computed using only the central segment of crack, taken as $x = 4$–12 mm. Results in Table IV clearly indicate that the larger the applied load, the earlier the crack propagation initiates, and the higher the average crack velocity.

In the experiment [6], velocity oscillation level increases with higher loading due to more frequent occurrence and longer length of microbranches. This trend can also be observed in the velocity profile, however, it is clouded by additional numerical issues. Consider loading cases $\varepsilon = 0.01$ and 0.015 for example. Since at lower loading rate ($\varepsilon = 0.01$) less microbranching occur

DOI: 10.1002/nme

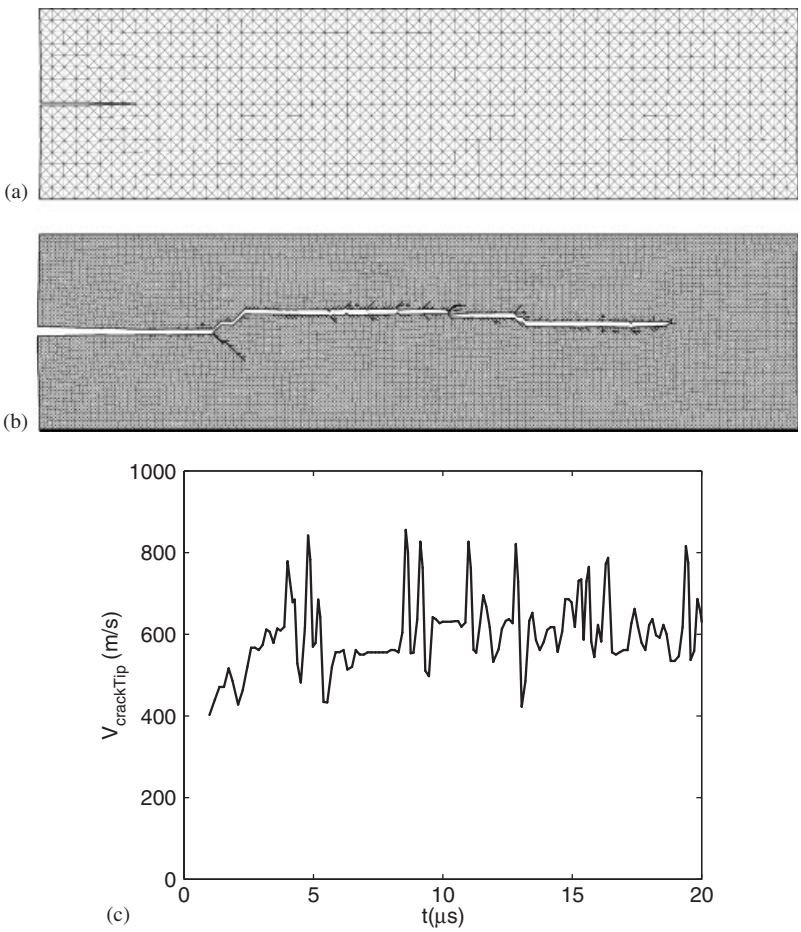

Figure 14. Mesh size influence on fracture pattern for applied stretch $\varepsilon = 0.01$: (a) crack arrests for coarse mesh (16×64 grid); (b) crack pattern for refined mesh (48×192 grid); and (c) associated crack velocity history for refined mesh (48×192 grid).

compared to higher loading ($\varepsilon = 0.015$), there are noticeably longer periods of smooth velocity history in the former case (Figure 14(c)) than in the latter (Figure 12(c), using the same 48×192 grid mesh). As for the velocity amplitude oscillation, both velocity profiles vary between 500 and 800 m/s, although the higher loading rate results in more peaks in the higher velocity amplitude than the lower loading rate case. A closer study of the velocity calculation and the microbranch pattern reveals that the computed velocity is highly sensitive to the insertion of each new cohesive element, when a sharp drop in the crack velocity history occurs. Since the crack velocity is computed as crack length variation over time step duration, it depends much on the choice of time step. In the present study, the time step is extremely small (of the order of 10^{-3} μs), and thus even though the crack length varies only marginally between two time steps, the calculated velocity variation is much amplified. Therefore, the high fluctuation in the velocity history is not only due to microbranching, but also to numerical artifacts.

DOI: 10.1002/nme

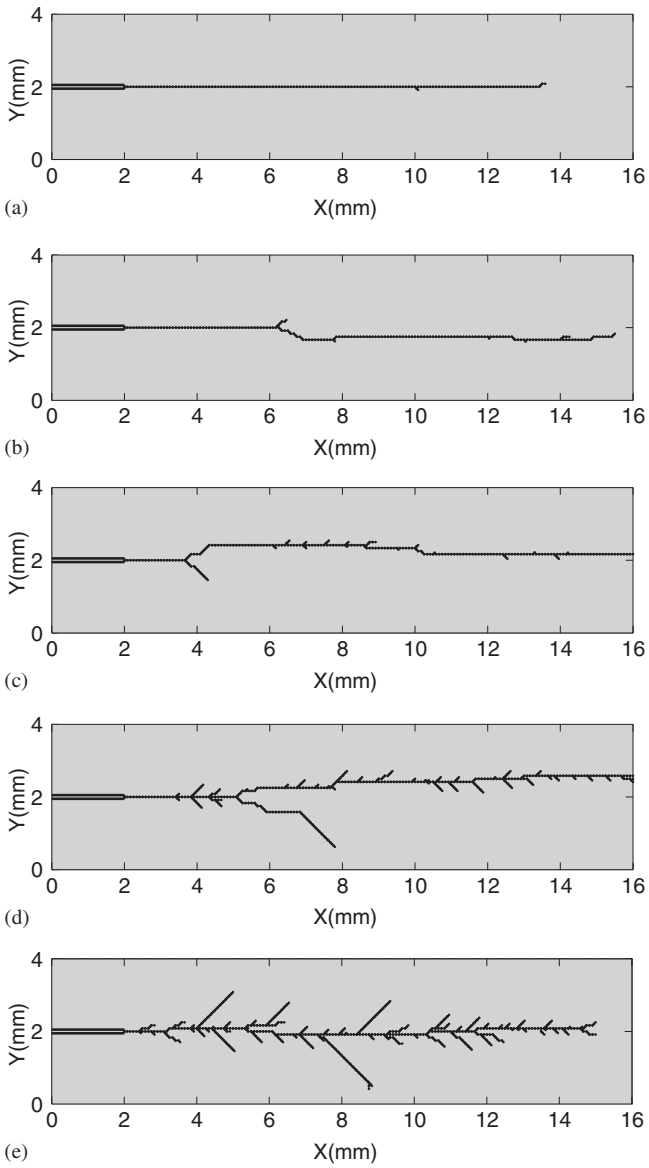

Figure 15. Comparison of branch patterns for various loading cases considering different applied strains (ε) and using an initial mesh discretization consisting of a 48×192 grid: (a) $\varepsilon = 0.0085$; (b) $\varepsilon = 0.009$; (c) $\varepsilon = 0.010$; (d) $\varepsilon = 0.012$; and (e) $\varepsilon = 0.015$.

6.6. Influence of check-time intervals for cohesive element insertion

The numerical results are influenced by the time intervals at which the cohesive element insertion criterion is checked. Since the evaluation of cohesive element insertion at each element edge at

DOI: 10.1002/nme

Table IV. Comparison of crack initiation time and average crack speed for different loading cases as shown in Figure 15.

Initial stretch ε	Mesh grids	Crack initiation time (μs)	Average crack velocity (m/s)
0.0085	48×192	1.61	518
0.009	48×192	1.23	558
0.010	48×192	0.98	572
0.012	48×192	0.71	597
0.015	48×192	0.47	642

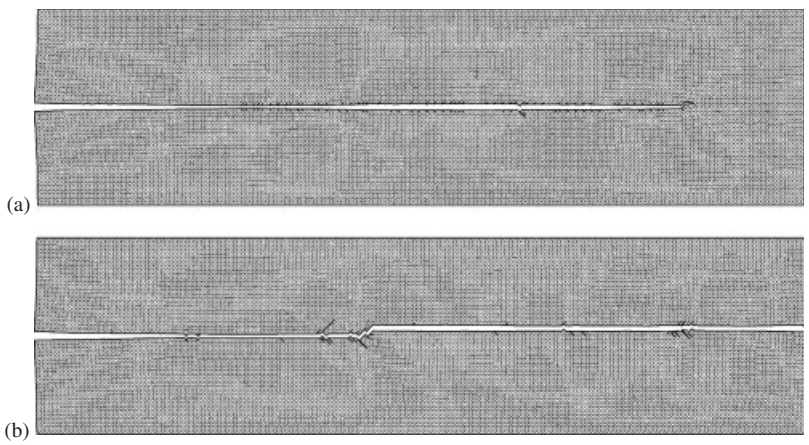

Figure 16. Comparison of branch patterns at $t = 19.8$ μs for applied initial stretch $\varepsilon = 0.0085$ using different cohesive element insertion checking intervals: (a) cohesive element insertion checked at every 10 time steps and (b) cohesive element insertion checked at every time step.

each time step is computationally heavy, the procedure is usually carried out every certain time steps. In this study, the results reported so far are obtained using a time step interval of 10, i.e. the cohesive element insertion is checked every 10 time steps. To evaluate the influence of this issue, further simulations are carried out in which cohesive element insertion check are performed at every time step. Two cases of interest are investigated, one with higher initial stretch ($\varepsilon = 0.0085$) and another with lower initial stretch ($\varepsilon = 0.008$).

Figures 16(a) and (b) compares the results with initial stretch of $\varepsilon = 0.0085$ using different time intervals. When cohesive element insertion is checked frequently (e.g. at each time step), upon satisfaction of the criterion, a new cohesive surface is introduced, and local stress concentration is released. In contrast, when cohesive element insertion is checked less frequently, although local stress around crack tip is high enough to initiate new interface, the cohesive element cannot be inserted immediately, and local stress builds up. Therefore at the time of cohesive element checking, more interfaces around the current crack tip may satisfy the separation criterion. Consequently, more microbranches form. This is revealed in Figure 16, which indicates that more microbranches (which are short and heal soon after the main crack runs forward) appear when cohesive element insertion is checked every 10 time steps (Figure 16(a)), compared to the case for which cohesive element insertion is checked at each time step (Figure 16(b)). More frequent check of cohesive elements also results in increased crack velocity, since the new crack surface does not need to 'wait'

DOI: 10.1002/nme

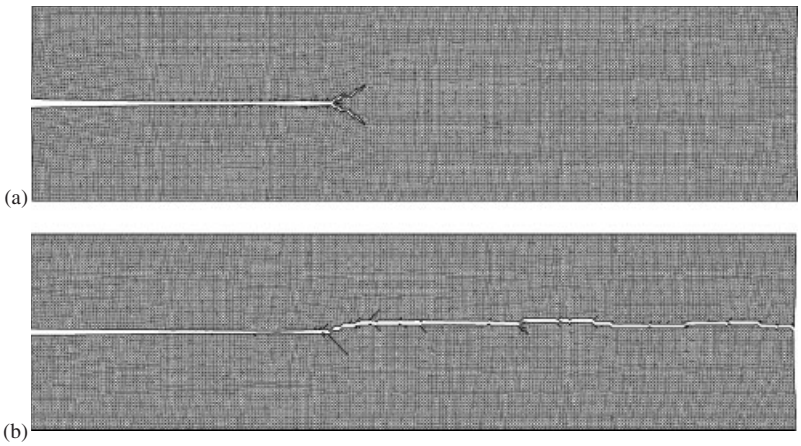

Figure 17. Comparison of branch patterns at $t = 25.4$ μs for applied initial stretch and $\varepsilon = 0.008$ using different cohesive element insertion checking intervals: (a) cohesive element insertion checked at every 10 time steps and (b) cohesive element insertion checked at every time step.

up to 10 time steps. Therefore, at time $t = 19.8$ μs, crack has run through the whole strip in Figure 16(b), but not in Figure 16(a). On the other hand, the overall crack patterns remain similar for this loading case.

In another test with initial stretch of $\varepsilon = 0.008$, the simulation results are different. Since this loading is relatively low, when two microbranches occur simultaneously (Figure 17(a)), the energy flowing into the two branches is divided into similar magnitude for each, and none is enough to drive the branch grow further. Consequently, both branches arrest. On the other hand, in Figure 17(b), simultaneous branches of similar strength did not occur, but one crack is dominant, and the crack propagates through the strip.

6.7. Energy evolution

Sharon and Fineberg [6] assumed that in the experiment carried out, all initial strain energy has been dissipated for fracture surface formation. At higher input energy, the apparent increase in fracture resistance is explained by the formation of ondulated crack surface and formation of significantly increased microbranches. The assumption is supported by the measurement of microcrack surface being proportional to the input energy. In the current study, we may not be able to make the same assumption, as the strain energy density is much higher in the reduced dimension problem in comparison to the original experiment. However, it is necessary to check the energy evolution history.

The energy components of interest are listed below, i.e.

- External work ($\mathscr{E}_{\text{ext}}$): work done by external loading.
- Kinetic energy (K): energy of motion.
- Strain energy due to elastic deformation of the bulk elements (U_{bulk}): elastic energy stored in the bulk material.
- Deformation energy due to elastic deformation of the cohesive elements (U_{coh}): elastic energy stored in the cohesive surfaces. This recoverable strain energy is depicted in Figure 18, where permanent damage and partial 'relaxation' of the interface have occurred.

DOI: 10.1002/nme

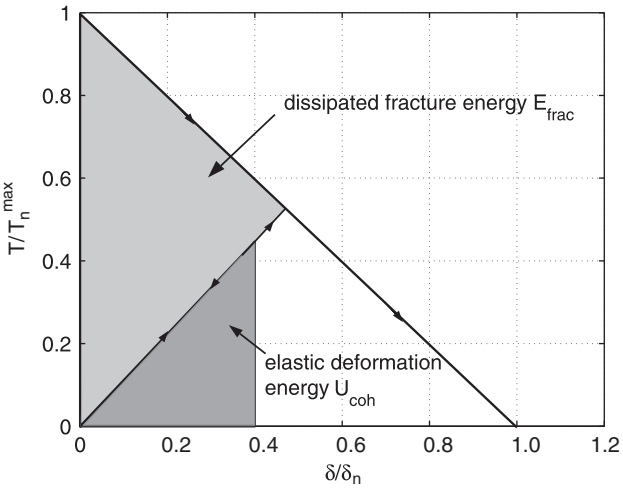

Figure 18. Components of the cohesive energy.

- Fracture energy ($\mathscr{E}_{\text{frac}}$): energy dissipated by the generation of new surfaces to form advancing crack(s).
- Total cohesive energy ($\mathscr{E}_{\text{coh}}$): sum of elastic cohesive energy (recoverable) and dissipated fracture energy (irrecoverable). $\mathscr{E}_{\text{coh}} = U_{\text{coh}} + \mathscr{E}_{\text{frac}}$.

For the current problem under discussion, the external work is kept constant, with value equal to the initial strain energy due to deformation. At any time instant, the total energy in the system is conserved, i.e.

$$\mathscr{E}_{\text{ext}} = \mathscr{E}_{\text{tot}} = U + K + \mathscr{E}_{\text{frac}} = \text{constant}, \quad U = U_{\text{bulk}} + U_{\text{coh}} \tag{12}$$

where U represents the total recoverable elastic energy of the system.

Figure 19 shows the evolution of various energy components for the crack propagation simulation in the PMMA strip with $\varepsilon = 0.008$, including the total elastic energy U, kinetic energy K, energy dissipated by fracture $\mathscr{E}_{\text{frac}}$. Apparently, part of the strain energy initially stored in the system gradually converts to fracture energy and drives the crack to propagate. A portion of strain energy is converted to kinetic energy, which oscillates in equilibrium with the strain energy. During the dynamic simulation, some elastic energy U_{coh} is stored in the cohesive elements, which consists only of a nominal fraction of the total recoverable energy U. The total cohesive energy $\mathscr{E}_{\text{coh}}$ can be decomposed into recoverable elastic part U_{coh} and dissipated fracture energy $\mathscr{E}_{\text{frac}}$.

Energy conservation is not perfectly retained in the numerical study, but is acceptable. Source of the error is the discontinuous nature of the cohesive model adopted. As can be seen in Figure 4, the traction–separation is discontinuous at separation close to 0. As fracture energy is numerically evaluated by summation of the integral of cohesive energy rate over time for each cohesive surface, the strong discontinuity results in inevitable error in the results. The error can be reduced by decreasing time step so as to better approximate the jump in the cohesive model, however, this

DOI: 10.1002/nme

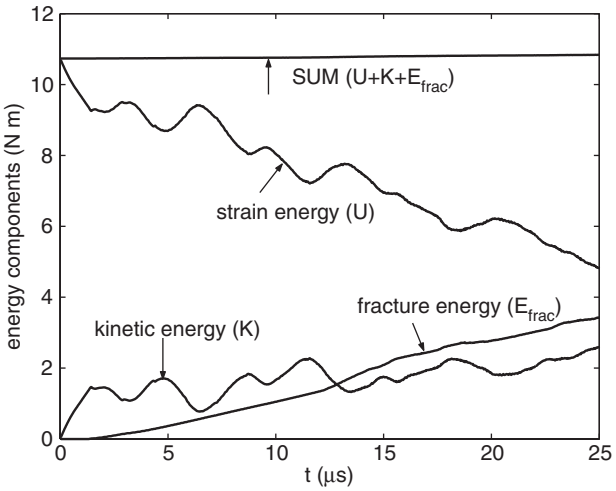

Figure 19. Energy components evolution with time for crack propagation problem with initial stretch $\varepsilon = 0.008$. Mesh used is 64×256 grids, cohesive element insertion is checked at every 10 time steps.

issue is innate to the numerical scheme and cannot be completely eliminated. A recent proposal for a time continuous CZM has been presented by Papoulia *et al.* [34].

7. CONCLUSIONS

In this study, dynamic microbranching in brittle materials is investigated using an *explicit* dynamic scheme and employing extrinsic cohesive zone elements to model fracture behaviour. This finite element framework is supported by a newly proposed [9] adjacency-based topological data structure (TopS), which provides efficient access to the geometrical and topological information necessary for the adaptive insertion of extrinsic cohesive elements.

Extrinsic CZM is employed in the investigation, which eliminates the undesirable artificial compliance associated with intrinsic CZM. The extrinsic model poses challenge both at the implementation stage and at the interpretation of simulation results. The numerical framework is carefully designed to interact with the data structure (TopS) so as to provide robust insertion of cohesive elements.

Numerical simulation is carried out based on a reduced dimension model of a dynamic fracture experiment on PMMA. The present work addresses neither explicit rate-dependent material behaviour nor localized heating effects at the crack tip of a propagating crack. Nonetheless, the numerical results reveal increased roughness of fracture surface, longer microbranches and higher crack speed for increased energy input, which is in accordance with those observed in the experiments. Various numerical issues are discussed in detail, including mesh convergence, cohesive element insertion check time intervals, as well as energy evolution. Apparently, the extrinsic model is successful in reproducing numerous crack microbranching occurrence. Compared to Miller *et al.*'s work [42], which employs a potential-based intrinsic CZM for the same problem, the present approach produces simulation results that resemble the experiment better with respect to

DOI: 10.1002/nme

both the microbranch angle and propagation length. This study thus reveals the importance of adopting extrinsic CZM approach when multiple local cohesive failure occurs in a large region.

ACKNOWLEDGEMENTS

We gratefully acknowledge the support from the National Center for Supercomputing Applications (NCSA) at the University of Illinois at Urbana-Champaign (UIUC). In addition, we would like to thank three anonymous reviewers for their valuable comments and informed suggestions, which contributed much to improve the manuscript. Any opinions, findings, conclusions or recommendations expressed in this publication are those of the authors and do not necessarily reflect the views of the sponsors.

REFERENCES

1. Cox BN, Gao H, Gross D, Rittel D. Modern topics and challenges in dynamic fracture. *Journal of the Mechanics and Physics of Solids* 2005; **53**:565–596.
2. Ravi-Chandar K, Knauss WG. An experimental investigation into dynamic fracture—I. Crack initiation and crack arrest. *International Journal of Fracture* 1984; **25**:247–262.
3. Ravi-Chandar K, Knauss WG. An experimental investigation into dynamic fracture—II. Microstructural aspects. *International Journal of Fracture* 1984; **26**:65–80.
4. Ravi-Chandar K, Knauss WG. An experimental investigation into dynamic fracture—III. On steady-state crack propagation and crack branching. *International Journal of Fracture* 1984; **26**:141–154.
5. Ravi-Chandar K, Knauss WG. An experimental investigation into dynamic fracture—IV. On the interaction of stress waves with propagating cracks. *International Journal of Fracture* 1984; **26**:189–200.
6. Sharon E, Fineberg J. Microbranching instability and the dynamic fracture of brittle materials. *Physical Reviews B* 1996; **54**:7128–7139.
7. Ravi-Chandar K, Yang B. On the role of microcracks in the dynamic fracture of brittle materials. *Journal of the Mechanics and Physics of Solids* 1997; **45**:535–563.
8. Celes W, Paulino GH, Espinha R. Efficient handling of implicit entities in reduced mesh representations. *Journal of Computing and Information Science in Engineering* 2005; **5**:348–359.
9. Celes W, Paulino GH, Espinha R. A compact adjacency-based topological data structure for finite element mesh representation. *International Journal for Numerical Methods in Engineering* 2005; **64**:1529–1556.
10. Yoffe EH. The moving Griffith crack. *Philosophical Magazine* 1951; **42**:739–750.
11. Freund LB. *Dynamic Fracture Mechanics*. Cambridge Monographs on Mechanics, Applied Mathematics, Batchelor FRS, Wushch C, Rice J (eds). Cambridge University Press: NY, 1990.
12. Gao H. Surface roughening and branching instabilities in dynamic fracture. *Journal of the Mechanics and Physics of Solids* 1993; **41**:457–486.
13. Rice JR, Ben-Zion Y, Kim K-S. Three-dimensional perturbation solution for a dynamic planar crack moving unsteadily in a model elastic solid. *Journal of the Mechanics and Physics of Solids* 1994; **42**:813–843.
14. Eshelby JD. Energy relations and the energy-momentum tensor in continuum mechanics. *In Inelastic Behaviour of Solids*, Kanninen WF, Rosenfield AR, Jaffe RI (eds). McGraw-Hill: New York, 1970; 77–115.
15. Freund LB. Crack propagation in an elastic solid subjected to general loading—I. Constant rate of extension. *Journal of the Mechanics and Physics of Solids* 1972; **20**:129–140.
16. Gao H. A theory of local limiting speed in dynamic fracture. *Journal of the Mechanics and Physics of Solids* 1996; **44**:1453–1474.
17. Abraham FF, Brodbeck D, Rafey RA, Rudge WE. Instability dynamics of fracture: a computer simulation investigation. *Physical Review Letters* 1994; **73**:272–276.
18. Xu X, Needleman A. Numerical simulations of fast crack growth in brittle solids. *Journal of the Mechanics and Physics of Solids* 1994; **42**:1397–1434.
19. Klein PA, Foulk JW, Chen EP, Wimmer SA, Gao H. Physics-based modeling of brittle fracture: cohesive formulations and the application of meshfree methods. *Technical Report SAND2001-8099*, Sandia National Laboratory, 2000.
20. Belytschko T, Chen H, Xu J, Zi G. Dynamic crack propagation based on loss of hyperbolicity and a new discontinuous enrichment. *International Journal for Numerical Methods in Engineering* 2003; **58**:1873–1905.

DOI: 10.1002/nme

21. Rafiee S, Seelig TH, Gross D. Simulation of dynamic crack curving and branching under biaxial loading by a time domain boundary integral equation method. *International Journal of Fracture* 2003; **120**:545–561.
22. Camacho GT, Ortiz M. Computational modeling of impact damage in brittle materials. *International Journal of Solids and Structures* 1996; **33**:2899–2938.
23. Barenblatt GI. The formation of equilibrium cracks during brittle fracture: general ideas and hypothesis, axially symmetric cracks. *Applied Mathematics and Mechanics (PMM)* 1959; **23**:622–636.
24. Barenblatt GI. The mathematical theory of equilibrium cracks. *Advances in Applied Mechanics* 1962; **7**:55–129.
25. Dugdale DS. Yielding of steel sheets containing cracks. *Journal of the Mechanics and Physics of Solids* 1960; **8**:100–104.
26. Bažant ZP, Cedolin L. *Stability of Structures*: *Elastic*, *Inelastic*, *Fracture and Damage Theories*. Oxford University Press: New York, 1991.
27. Bažant ZP, Planas J. *Fracture and Size Effect in Concrete and Other Quasibrittle Materials*. CRC Press: New York, 1998.
28. Geubelle PH, Baylor J. Impact-induced delamination of laminated composites: a 2D simulation. *Composites Part B Engineering* 1998; **29**:589–602.
29. Zavattieri P, Espinosa H. Grain level model analysis of crack initiation and propagation in brittle materials. *Acta Materialia* 2001; **49**:4291–4311.
30. Pandolfi A, Ortiz M. An efficient adaptive procedure for three-dimensional fragmentation simulations. *Engineering with Computers* 2002; **18**:148–159.
31. Needleman A. A continuum model for void nucleation by inclusion debonding. *Journal of Applied Mechanics* 1987; **54**:525–531.
32. Tvergaard V. Effect of fiber debonding in a whisker-reinforced metal. *Materials Science and Engineering A* 1990; **125**:203–213.
33. Ortiz M, Pandolfi A. Finite-deformation irreversible cohesive elements for three-dimensional crack-propagation analysis. *International Journal for Numerical Methods in Engineering* 1999; **44**:1267–1282.
34. Papoulia KD, Sam CH, Vavasis SA. Time continuity in cohesive finite element modeling. *International Journal for Numerical Methods in Engineering* 2003; **58**:679–701.
35. Falk ML, Needleman A, Rice JR. A critical evaluation of cohesive models of dynamic fracture. *Journal de Physique IV* 2001; **11**:Pr5—43–50.
36. Zhang Z, Paulino GH. Cohesive zone modeling of dynamic failure in homogeneous and functionally graded materials. *International Journal of Plasticity* 2005; **21**:1195–1254.
37. Repetto EA, Radovitzky R, Ortiz M. Finite element simulation of dynamic fracture and fragmentation of glass rods. *Computer Methods in Applied Mechanics and Engineering* 2000; **183**:3–14.
38. Belytschko T, Liu WK, Moran B. *Nonlinear Finite Elements for Continuua and Structures*. Wiley: New York, 2000.
39. Bathe K-J. *Finite Element Procedures*. Prentice-Hall: NJ, 1996.
40. Belytschko T, Chiapetta RL, Bartel HD. Efficient large scale non-linear transient analysis by finite elements. *International Journal for Numerical Methods in Engineering* 1976; **10**:579–596.
41. Sharon E, Gross SP, Fineberg J. Energy dissipation in dynamic fracture. *Physical Review Letters* 1995; **76**: 2117–2120.
42. Miller O, Freund LB, Needleman A. Energy dissipation in dynamic fracture of brittle materials. *Modelling and Simulation in Materials Science and Engineering* 1999; **7**:573–586.
43. Sharon E, Gross SP, Fineberg J. Local crack branching as a mechanism for instability in dynamic fracture. *Physical Review Letters* 1995; **74**:5096–5099.
44. Rice JR. Mathematical analysis in the mechanics of fracture. In *Fracture*, *an Advanced Treatise*, Liebowitz (ed.), vol. 2. Academic Press: New York, 1968; 191–311.
45. Pandolfi A, Krysl P, Ortiz M. Finite element simulation of ring expansion and fragmentation. *International Journal of Fracture* 1999; **95**:279–297.
46. Pandolfi A, Guduru PR, Ortiz M, Rosakis AJ. Three dimensional cohesive-element analysis and experiments of dynamic fracture in C300 steel. *International Journal of Solids and Structures* 2000; **37**:3733–3760.
47. Zhang Z. Cohesive zone modeling of dynamic failure in homogeneous and functionally graded materials. *Master Thesis*, University of Illinois at Urbana-Champaign, 2003.

DOI: 10.1002/nme